NJC

ROYAL SOCIETY OF CHEMISTRY

PAPER

View Article Online
View Journal | View Issue

Cite this: *New J. Chem.*, 2024, **48**, 15402

A highly specific benzothiazole-based Schiff base for the ratiometric detection of hypochlorite (ClO^-) ions in aqueous systems: a real application in biological imaging†

Aastha Palta,[a] Sunidhi Sharma,[a] Gulshan Kumar,[b] Diptiman Choudhary,[a] Kamaldeep Paul[a] and Vijay Luxami*[a]

Received 26th April 2024,
Accepted 1st August 2024

DOI: 10.1039/d4nj01933d

rsc.li/njc

This study describes the rational development and synthesis of a benzothiazole-salicylaldehyde Schiff base **probe 1**. This probe is designed to function as a ratiometric fluorescent probe specifically for detecting ClO^- ions, utilizing the imine bond as the fluorophore unit. Upon interaction with ClO^- ions, **probe 1** exhibits a redshift in its absorption spectrum from 435 nm to 450 nm. Moreover, in its emission spectrum, there is a ratiometric emission enhancement observed at 610 nm, providing a clear indication of the presence of ClO^- ions. The sensitivity of **probe 1** for detecting ClO^- ions is quantified, revealing a lowest detection limit of 5.5 μM, indicating its potential for sensitive detection even at low concentrations of ClO^- ions. Additionally, it has been successfully utilized for biological imaging purposes, demonstrating low cytotoxicity, which is crucial for its applicability in biological systems.

1. Introduction

Hypochlorite ions are commonly used in everyday products like disinfectants and household bleach, and in cyanide treatment.[1] They are typically utilized within a concentration range of 10^{-2}–10^{-5} M. Higher concentrations of hypochlorite solutions pose a potential health hazard to living systems, indicating the importance of proper handling and dilution.[2] Hypochlorite ions are categorized as reactive oxygen species (ROS),[3,4] along with other molecules like hydroxyl radicals, hydrogen peroxide, and superoxide radicals. ROS play significant roles in living systems, but their imbalance can lead to oxidative stress and damage.[5–7] Hypochlorous acid (HOCl) and hypochlorite ions (ClO^-, a conjugate base) are essential reactive oxygen species, generated endogenously during microbial invasion *in vivo*, particularly through the catalytic action of the myeloperoxidase (MPO) enzyme in leukocytes.[8–11] ClO^- exhibits antibacterial activity and aids in tissue repair when tissues are injured.[12] However, excessive levels can lead to tissue damage and contribute to various diseases such as arthritis, cancer, cardiovascular disease, kidney disease, and environmental pollution.[13–18] Given the importance of maintaining ClO^- concentrations within a balanced range, there's a need to develop effective techniques for determining ClO^- concentration in physiological functions induced by ClO^- in living systems.

Fluorescence probes offer high selectivity, sensitivity and real-time monitoring for detecting ClO^- ions, making them effective tools for accurate measurement even at low concentrations. The use of fluorescence probes offers a straightforward detection procedure, simplifying the experimental process.[19–21] Organic fluorescence probes, in particular, are highlighted for their fast reaction time, simple synthesis, and fluorescence output signal, which make them suitable for real-time investigation of ClO^- levels.[22–25] Small molecular probes, including organic fluorescence probes, are extensively utilized in chemical analysis and environmental detection due to their effectiveness and practicality. Additionally, these probes find applications in medicine, underscoring their significance in various fields beyond environmental monitoring.[26,27]

Numerous fluorescent probes capable of sensing ClO^- ions have been reported. These probes vary in their targeting, including some designed to interact with subcellular organelles. Fluorescence probes for ClO^- ions can be categorized based on their binding mechanisms and binding sites. Examples include probes utilizing C=C unsaturated bonds as recognition groups[28–31] and those containing nitrogen atoms and chalcogenide elements (sulfur, selenium, tellurium, *etc.*).[32–34] Developing and synthesizing probes for ClO^- ions poses several challenges. One major obstacle is the short lifespan of ClO^- ions in complex cellular environments,

[a] *Department of Chemistry and Biochemistry, Thapar Institute of Engineering and Technology, Patiala-147004, India. E-mail: vluxami@thapar.edu*
[b] *Department of Chemistry, Banasthali University, Banasthali Newai 304022, Rajasthan, India*

† Electronic supplementary information (ESI) available. See DOI: https://doi.org/10.1039/d4nj01933d

necessitating real-time detection methods. There is a high demand for real-time detection of ClO^- ions to better understand their roles in significant biological processes. To meet the demands of biological research, an ideal probe for ClO^- ions should possess characteristics such as high specificity, low detection limit, rapid response time, and minimal cytotoxicity. However, numerous options still exhibit drawbacks, including complex synthetic processes and challenges in conducting *in vivo* experiments. Therefore, it is imperative to design easily accessible colorimetric and fluorescent chemosensors for detecting ClO^- in biological systems. Nonetheless, certain alternatives suffer from poor water solubility and high toxicity *in vivo*.[35]

The synthesized probe is based on the benzothiazole unit, which likely contributes to its selectivity and sensitivity for ClO^- ions. The introduction of the $-NEt_2$ group induces an inductive effect, leading to the generation of a $\delta+$ charge on the carbon atom of the imine bond. This structural modification likely facilitates hydrolysis by HOCl, enabling the detection of ClO^- ions. This probe exhibits excellent selectivity and high sensitivity for ClO^- ions, allowing for accurate detection even in mixed aqueous solutions. The emission maximum of the probe shows quenching with a small red shift in the band upon the addition of ClO^- ions, indicating its responsiveness to ClO^- concentration changes. The lowest detection limit for ClO^- ion detection with **probe 1** is determined to be 5.5 μM, indicating its capability to detect low concentrations of ClO^- ions. **Probe 1** is effectively utilized for biological imaging, suggesting its potential utility in visualizing ClO^- ions within biological systems. Additionally, the probe exhibits low cytotoxicity, which is crucial for its application in biological imaging without causing harm to living cells.

2. Experimental section

2.1. Materials and characterizations

All the reactions were carried out using the commercially available reagents obtained from Sigma-Aldrich and Spectrochem Pvt. Ltd, India and used without any purification unless stated otherwise. Reactions were monitored using thin-layer chromatography (TLC), which was performed on silica plates coated with silica gel HF-254 purchased from Spectrochem Pvt. Ltd, India. TLCs were seen with UV light (254 or 365 nm) or I_2 staining. Purifications were carried out by column chromatography using SiO_2 (60–120 mesh). ^1H and ^{13}C NMR spectra were recorded on a Bruker 400 MHz spectrometer (^1H NMR at 400 MHz, ^{13}C NMR at 100 MHz). Chemical Shifts were expressed in parts per million with TMS as an internal reference and residual peaks for deuterated solvents are $CDCl_3$ at 7.26 ppm, and DMSO-d_6 at 3.33 ppm or 2.50 ppm. The following abbreviations are used to represent the NMR data (s, singlet; d, doublet; t, triplet; q, quartet; dd, doublet of doublets; m, multiplet). The mass spectrum of the synthesized molecule was carried out using an XEVO G2-XS QTOF spectrometer.

The stock solution of **probe 1** was prepared in CH_3CN at 10^{-3} M concentration and was further diluted as required for photophysical studies. The absorption studies were carried out on a SHIMADZU-2600 machine using a quartz cell of 1 cm path length. The fluorescence studies were performed on a Varian Carey Eclipse spectrophotometer using slit width (excitation-5 nm, emission-5 nm) at the stated excitation. All absorption and emission scans were saved as ACS files and later converted in excel™ to produce the graphs. The DFT studies were performed in Gaussian 16 software using the B3LYP/6-31G* basis set. Stock solutions for the anions of 10^{-1} M concentration, *viz.* F^-, CN^-, Cl^-, Br^-, I^-, SCN^-, AcO^-, NO_3^-, $P_2O_7^{4-}$, $H_2PO_4^-$, and HSO_4^-, were prepared from their tetrabutyl ammonium salts in deionized water and these were also further diluted as per the requirement. The deionized water was used for the preparation of HEPES buffer (10 mM) solution.

Ham's F1-2 medium, fetal bovine serum, 100 × penicillin–streptomycin solutions, and 3-(4,5-dimethylthiazol-2-yl)-2.5-diphenyltetrazolium bromide (MTT) were purchased from Himedia, India. Molecular biology grade chemicals such as sodium hydroxide, formaldehyde, dimethyl sulphoxide, hydrochloric acid, sodium bicarbonate, *etc.*, were purchased from Loba Chemie, India.

2.2. Synthesis of probe 1

Compound **1a**[36] and *N*,*N*-diethylamino salicylaldehyde were refluxed in ethanol for 8 h (Scheme 1). On completion, the reaction mixture was cooled and the solid was filtered, and further washed with ethanol to get a yellowish green colored solid of **probe 1** in 80% yield. M.pt. 275–280 °C. ^1H NMR ($CDCl_3$-d_6, 400 MHz): δ (ppm) 12.6 (bs, 1H, OH), 8.45 (s, 1H, CH), 7.96 (d, 1H, J = 8 Hz, ArH), 7.89 (d, 1H, J = 8 Hz, ArH), 7.67 (d, 1H, J = 8 Hz, ArH), 7.51 (t, 1H, J = 16 Hz, ArH), 7.40 (t, 1H, J = 16 Hz, ArH), 7.17 (d, 1H, J = 8 Hz, ArH), 6.93 (d, 1H, J = 4 Hz, ArH), 6.85 (dd, 1H, J_1 = 8 Hz, J_2 = 12 Hz, ArH), 6.27 (dd, 1H, J_1 = 4 Hz, J_2 = 8 Hz, ArH), 6.18 (d, 1H, J = 4 Hz, ArH), 3.43 (q, 4H, J = 12 Hz, eth-CH_2), 1.22 (t, 6H, J = 8 Hz, eth-CH_3) (Fig. S1, ESI†). ^{13}C NMR (DMSO-d_6, 100 MHz): δ (ppm) 191.2, 180.8, 179.1, 177.6, 174.3, 173.4, 163.9, 162.8, 160.8, 157.4, 154.3, 151.8, 151.5, 140.1, 137.7, 132.7, 126.0, 73.2, 41. 2 (Fig. S2, ESI†). ESI-MS: m/z 418.16 (M^+ + 1) (Fig. S3, ESI†).

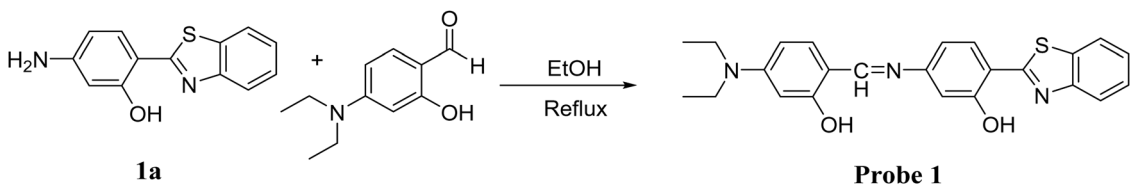

Scheme 1 Synthesis of **probe 1**.

2.3. NMR titration procedure

^{1}H NMR titrations of **probe 1** against NaOCl were carried out in CD_3OD-d_4 at 5 mM concentration using a JEOL ECS-400MHz spectrophotometer. All the recorded data were then processed in Mestronova software to draw the stacking data of **probe 1** and **probe 1** + NaOCl at different concentrations.

2.4. Detection limits

The detection limit (DL) is determined from the following eqn (1):

$$\mathrm{DL} = \frac{K \times \text{standard deviation of the blank solution}}{\text{slope of calibration curve}} \quad (1)$$

2.5. Cell viability assay

The cytotoxicity of **probe 1** and NaOCl was checked using the MTT assay, where the A549 lung cancer cell line (ATCC No. CCL-185) was cultured in Ham's F-12 media and supplemented with 10% fetal bovine serum (FBS), antibiotics, and anti-fungal. These cells were maintained at 37 °C with 5% CO_2 and humidified conditions in T25 cell culture flasks.[37,38] Later, these cells were seeded in 96 well plates at a cell density of 3×10^4 cells per well and incubated with different concentrations of **probe 1** (1, 5, 10, 25, 50 μM) and NaOCl (1, 10, 25, 50, 100 μM) alone or in combination for 24 h. For combination, various concentrations of **probe 1** (10, 25, and 50 μM) were incubated in combination with sodium hypochlorite (5, 10, 25, 50 μM). After incubation, 10 μl of MTT solution was added to each well at a concentration of 0.2 mg ml^{-1} and incubated for another 3 h. The purple-colored formazan crystals formed were then dissolved in DMSO, and the absorbance was measured using an ELISA plate reader (PowerWave XS2, BioTek) at 570 nm.[39] All the data were taken from the mean of 3 independent experiments, and % cell viability was calculated using eqn (2).

$$\%\ \text{cell viability} = \frac{\text{OD of treated cells}}{\text{OD of untreated cells}} \times 100\% \quad (2)$$

2.6. *In vitro* bio-imaging

The *in vitro* bio-imaging for the sensing of hypochlorite was done using the A549 cell line. To start with, A549 cells were seeded on sterile glass coverslips on 35 mm cell culture dishes at a cell density of 5×10^5 cells per ml and incubated overnight in Ham's F12 media.[40] For the treatment, aqueous NaOCl solution was used as an extrinsic hypochlorite (ClO^-) source where the cells were pre incubated with different concentrations of hypochlorite (1.0, 2.5, 5.0, 7.5, 10.0 μM). The pretreated cells were later treated with **probe 1** (30 μM) in Ham's F12 media containing 10% fetal bovine serum. The experiment was performed in triplicate and the treated cells were incubated for 3 h at 37 °C in the presence of 5% CO_2. The cells were later washed with 1× PBS buffer and fixed in 2% formaldehyde solution. The change in fluorescence was checked under the microscope using violet and green excitation light at 20× magnification. Images were captured using a Dwinter Inverted Fluorescence Microscope, Italy. The pixel intensity of green and red fluorescence obtained was calculated using Image J software, and further processing was done using Microsoft Excel. Repeated measures ANOVA followed by Tukey's HSD posthoc test were performed where a 10 × 10 pixel area of the image was measured and the pixel intensity values were used for the repeated measures to check the change in fluorescence pattern. Two measurements were considered statistically significant if the corresponding p-value was <0.01.[41]

3. Results and discussion

3.1. Photophysical studies of probe 1

At ambient temperature, the UV-Vis and fluorescence spectra of **probe 1** (20 μM) were recorded in different polar, nonpolar, protic and aprotic solvents. The **probe 1** showed absorption and emission maxima at 410 nm and 500 nm, respectively (Fig. 1a). In all the solvents, **probe 1** showed an absorption band in the range of 380–450 nm due to π–π* transition (Fig. 1b). **Probe 1** showed red shift of 70 nm in the absorption intensity from 380 nm to 450 nm on increasing the polarity of the solvent (Fig. 2a). Similarly, **probe 1** showed an emission band in the range of 500–510 nm in all the solvents. As the polarity of the solvent is increased, the fluorescence intensity also increases with a slight red shift in the emission maxima from 500 nm to 510 nm (Fig. 2b), associated with visible emission color changes under UV light (Fig. 2, inset). The slight variation in the

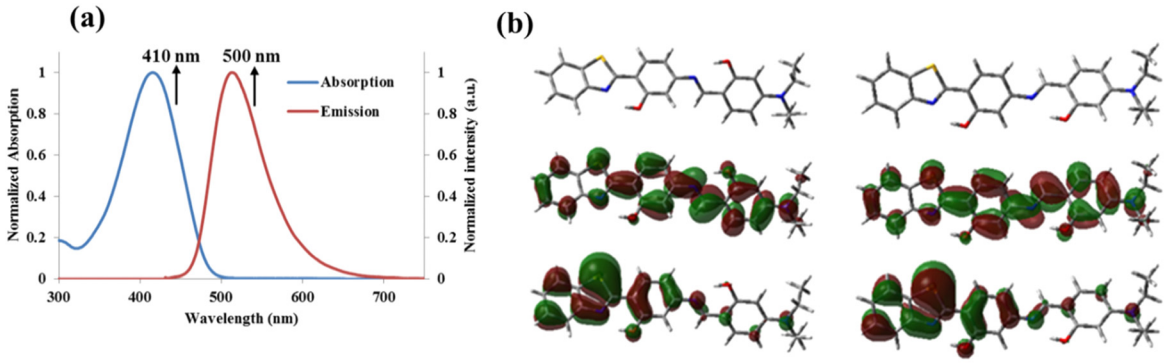

Fig. 1 (a) Normalized absorption and emission spectra of **probe 1** (20 μM, CH_3CN; λ_{ex} = 410 nm) and (b) optimized structure of **probe 1**.

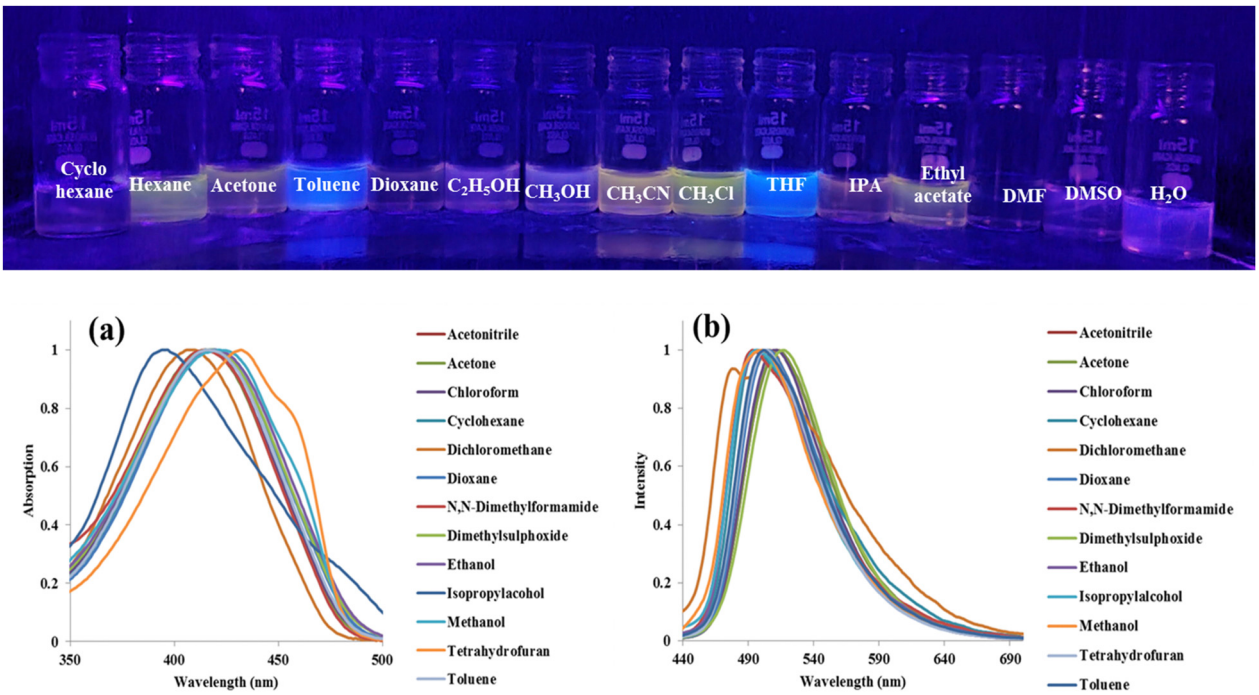

Fig. 2 (a) Absorption and (b) emission spectra of **probe 1** in different polarity solvents; Inset: The color change image of **probe 1** in different polarity solvents under UV light.

emission band could be due to the differential stabilization of the emission band by different solvents in the excited state.

3.2 Ground state structure, electronic distribution, and intramolecular proton transfer or charge transfer

We optimized **probe 1** and examined the possibilities of different configurations. Potential energy curves were constructed for C=N rotation (imine center connection). Torsional rotation around the C=N unit has an energy barrier of 1.73 kcal mol^{-1} in the S_0 state, which is less than the thermal energy of 5 kcal mol^{-1} and thus, signifies the coexistence of **probe 1-C1** and **probe 1-C2** configurations that can be interconvertible in the S_0 state (Fig. 3a). The Boltzmann populations were determined to be 34%, and 66% for **probe 1-C1**, and **probe 1-C2** configurations. **Probe 1-C1** and **probe 1-C2** have no imaginary frequencies and slightly twisted geometry in the S_0 state. The interconvertible nature of the configurations was also determined through PEC in the S_1 state and it was found that the energy barriers have high values in the S_1 state and thus, do not allow interconversion.

This study has been done with optimized **probe 1** and different configurations were explored, focusing on C=N rotation. The potential energy curves showed a 1.73 kcal mol^{-1} energy barrier in the S_0 state (which is less than thermal energy of 5 kcal mol^{-1}), indicating co-existence and interconvertible configurations. The determined Boltzmann populations were 34% and 66% for **probe 1-C1** and **probe 1-C2**, respectively. Interconvertibility was determined through PEC in the S_1 state, but the energy barriers were high, preventing interconversion.

Furthermore, three low-lying **probe 1** excitations, corresponding to the S_0 geometry, were calculated to investigate the absorption spectra source, with a summary in Table 1. **Probe 1-C1** exhibits an oscillation strength of 2.0153 at 346 nm, indicating 84% orbital transition contribution from the highest occupied molecular orbital to the lowest unoccupied molecular orbital. The study focuses on the $S_0 \rightarrow S_1$ excitation at 288 nm and 272 nm, as the second and third excitations have weak oscillation strength (Table 1).

The electron density in the relevant molecular orbitals changed from the benzothiazole unit (HOMO) to the Schiff base unit (LUMO) (Fig. 3b). The subsequent orbital composition also supported the electron density shift from the HOMO (majorly localized over S_8 (49.42%), C_2 (6.25%), C_4 (7.75%), C_6 (6.32%), and C_9 (7.97%)) to the LUMO (S_8 (3.41%), C_2 (0.23%), C_4 (0.84%), C_6 (2.49%), C_9 (2.83%), C_{10} (6.58%), C_{17} 6.46%, C_{19} (8.18%), N_{21} (7.65%), C_{22} (20%), and C_{24} (8.22%), and C_{28} (6.60%)) evoking intramolecular charge transfer from the benzothiazole unit to the Schiff base and diethylamino units. Additionally, the hole–electron analysis showed a small overlap integral (S_r = 0.5191) and significantly distant (D = 5.836 Å) hole–electron centroid, suggesting an intramolecular charge transfer process. The **Probe 1-C2** configuration also showed a similar pattern of behavior, as shown in Fig. 3b and Table 1.

Furthermore, the study identifies the presence of two types of asymmetrical intramolecular hydrogen bonding (IraHB) in **probe 1**, $O_{30}H_{43}\cdots N_7$ and $O_{29}H_{42}\cdots N_{21}$, with a short distance of 1.741 Å and 1.718 Å, respectively, which are essential for understanding the probe's behavior in the ESIPT process (Fig. 4a). Furthermore, the proton transferred tautomeric forms (EE, EK1, EK2, KK) were optimized and corrected for zero-point energy. It was determined that the enol form was found to be

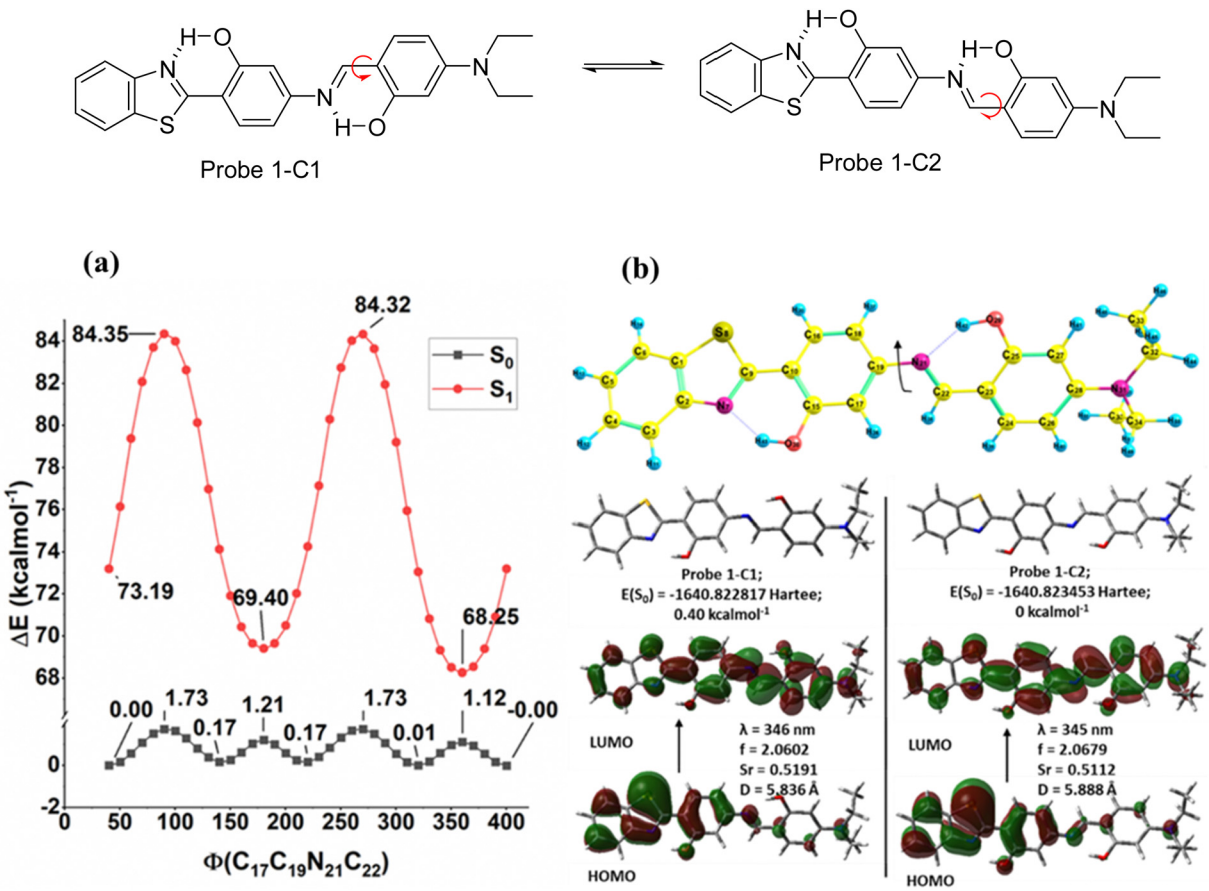

Fig. 3 (a) Energy profile for the torsional rotation optimized structure and (b) frontier molecular orbitals for $S_0 \rightarrow S_1$ excitation.

Table 1 Summary of excitation spectra of **probe 1** for the **probe 1-C1** and **probe 1-C2** configuration

	Probe 1-C1			**Probe 1-C2**		
$S_0 \rightarrow S_n$	λ (nm)	F	Molecular orbital	λ (nm)	f	Molecular orbital
$S_0 \rightarrow S_1$	346.79	2.0602	H → L (66%) H−1 → L (14%)	345.25	2.0679	H → L (65%) H−1 → L (14%)
$S_0 \rightarrow S_2$	296.25	0.0091	H−1 → L (52%) H → L+1 (20%)	295.99	0.0231	H−1 → L (50%) H → L+1 (20%)
$S_0 \rightarrow S_3$	272.49	0.0459	H−2 → L (32%) H−1 → L+1 (30%) H → L+4 (17%)	272.92	0.0559	H−2 → L+1 (25%) H−2 → L (25%) H−3 → L (17%)

λ = estimated excitation wavelength (nm); H = HOMO; L = LUMO.

the most stable form in the S_0 and S_1 state for both the **probe 1-C1** and **probe 1-C2** configurations. The energy profile established a relationship of EE (0 kcal mol^{-1}) > EK1 (0.02 kcal mol^{-1}) > EK2 (6.54 kcal mol^{-1}) > KK (6.06 kcal mol^{-1}) in the S_0 state and EE (68.25 kcal mol^{-1}) < EK1 (68.61 kcal mol^{-1}) < EK2 (72.65 kcal mol^{-1}) < KK (72.0 kcal mol^{-1}) in the S_1 state for **probe 1-C1**. Similarly for **probe 1-C2**, the energy relationship of EE (0 kcal mol^{-1}) > EK1 (0.05 kcal mol^{-1}) > EK2 (6.95 kcal mol^{-1}) > KK (6.18 kcal mol^{-1}) in the S_0 state and EE (69.23 kcal mol^{-1}) < EK1 (69.45 kcal mol^{-1}) < EK2 (74.43 kcal mol^{-1}) < KK (74.08 kcal mol^{-1}) in the S_1 state was established. The above mentioned energy relationship rejects the existence of an ESIPT process for **probe 1** in both configurations. The non-existence of the ESIPT process was measured due to the increase of the atomic contribution of O_{29} and H_{42} (0.11% → 0.99% for O_{29} and 0.027% → 0.071% for H_{42}), for $O_{29}H_{42}\cdots N_{21}$ and the decrease of N_7 (3.30% → 1.96%) for $O_{30}H_{43}\cdots N_7$ on HOMO → LUMO transition, that do not allow proton efficiency.

Probe 1 exhibited intramolecular charge transfer characteristics that could occur *via* planar or twisted intramolecular charge transfer. The possibility of twisted intramolecular proton transfer was determined through PECs *via* torsional rotation at C–N rotations (at diethylamino unit connections). Twisted forms have high energy and require energy as a barrier

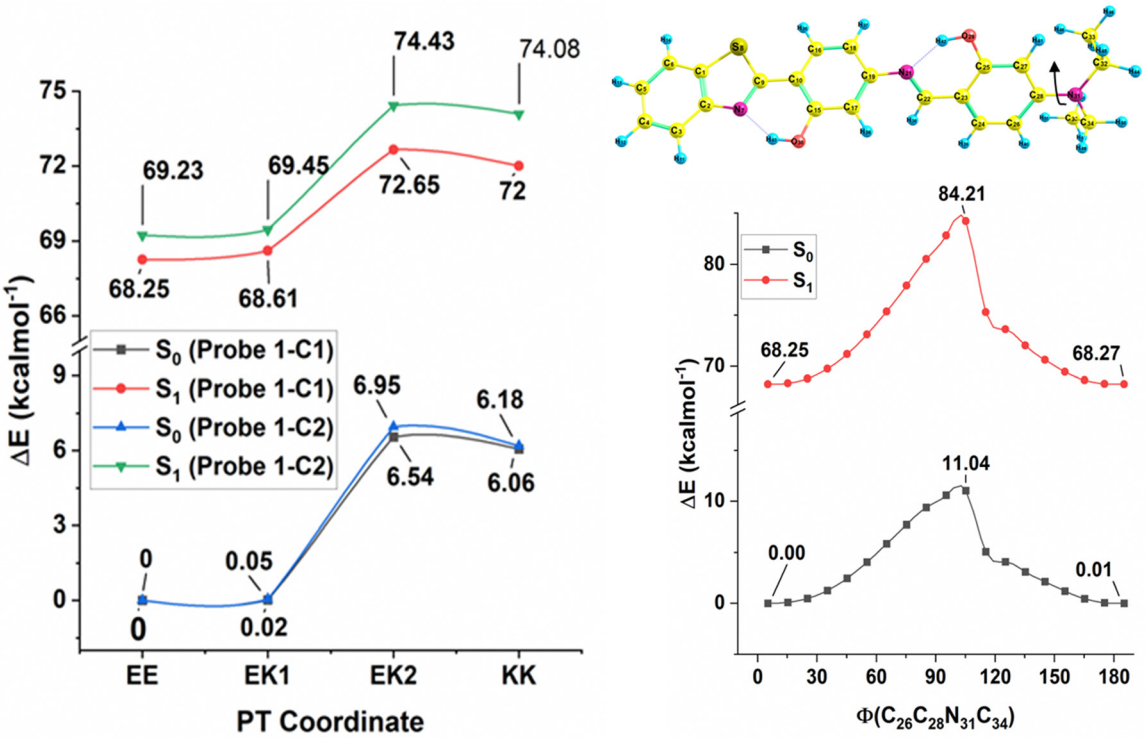

Fig. 4 Energy profile of tautomeric conversion and rotation at the diethylamino center in the S_0 and S_1 states.

for conversion, allowing only planar intramolecular charge transfer. This was confirmed through PECs *via* torsional rotation at C–N rotations. The twisted forms, with their high energy, require energy as a barrier for conversion, allowing only planar intramolecular charge transfer.

3.3. UV-Vis response of probe 1 towards anions

In order to determine the sensing ability of chromogenic detection of **probe 1**, UV-Vis spectra of **probe 1** (20 μM) in the absence and presence of different anions (F^-, CN^-, Br^-, I^-, SCN^-, AcO^-, ClO^-, ClO_4^-, NO_3^-, $P_2O_7^{4-}$, $H_2PO_4^-$, HSO_4^-, H_2O_2 and SO_4^{2-}) were recorded in $CH_3OH:H_2O$ (9 : 1, [v/v], pH = 7.04). **Probe 1** showed its absorption maximum at 435 nm. Upon addition of ClO^- (1000 μM) to the solution of **probe 1**, a red shift along with an increase in absorption intensity was observed (Fig. 5a). However, in the presence of competing anions, no significant change in the absorption spectra was observed. With the gradual addition of ClO^- ions to **probe 1**, the absorption band at 450 nm increases (Fig. 5b) and a plateau was observed after the addition of 0–200 μM of ClO^- ions. The detection limit of **probe 1** for ClO^- ions was found to be 1.5×10^{-6} M.

3.4. Fluorescence response of probe 1 towards anions

To further investigate the sensing ability, the fluorescence response of **probe 1** towards different anions (F^-, CN^-, Br^-, I^-, SCN^-, AcO^-, ClO^-, ClO_4^-, NO_3^-, $P_2O_7^{4-}$, $H_2PO_4^-$, HSO_4^-, H_2O_2 and SO_4^{2-}) was examined in $CH_3OH:H_2O$ (9 : 1, [v/v],

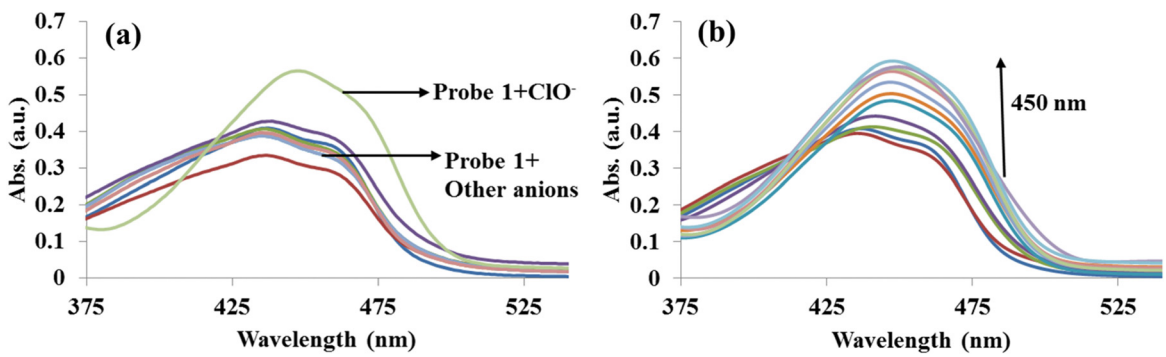

Fig. 5 Absorption spectra of **probe 1** (20 μM) $CH_3OH:H_2O$ (9 : 1, [v/v], pH = 7.04), (a) in the presence of different anions (1000 μM) and (b) with incremental addition of 0–200 μM of ClO^- ions.

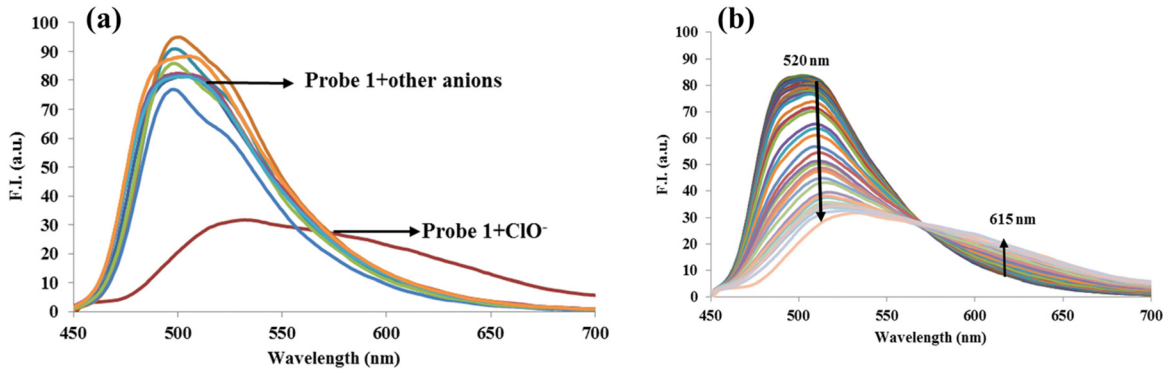

Fig. 6 Emission spectra of **probe 1** (20 μM) $CH_3OH:H_2O$ (9 : 1, [v/v], pH = 7.04), (a) in the presence of different anions (1000 μM) and (b) with incremental addition of 0–300 μM of ClO^- ions.

pH = 7.04) at 20 μM concentration. The free **probe 1** solution showed blue fluorescence at 500 nm on excitation at 435 nm, which could be due to the radiation-less deactivation by fast imine bond isomerization. The **probe 1** showed fluorescence quenching behavior after the addition of ClO^- ions with a bathochromic shift to 615 nm over the other tested anions (Fig. 6a). A plateau in the fluorescence spectra was observed after the addition of 300 μM of ClO^- ions (Fig. 6b). To further test whether **probe 1** can selectively detect ClO^- ions even in the presence of other anions, a competitive ion experiment was carried out. **Probe 1** was treated with other anions in the presence of ClO^- ions. The results indicated that the other ions do not lead to any significant change in the fluorescence intensity and the ClO^- ions showed the same spectral change even in the presence of other competitive anions. The fluorescence response to the addition of ClO^- ions was not affected by the presence of other commonly coexisting anions, indicating the selectivity of **probe 1** towards ClO^- ions (Fig. S4, ESI†).

3.5. Sensitivity of probe 1 towards ClO^- ions

To further check the sensitivity of **probe 1** towards ClO^- ions, we determined the lowest detection limit of **probe 1** with ClO^- ions. The lowest detection limit for the **probe 1**-ClO^- complex was 5.5×10^{-6} M.

3.6. ^{1}H NMR titrations

In order to investigate the binding behavior of **probe 1** towards ClO^- ions, we performed ^{1}H NMR titrations in CD_3OD-d_4. Upon

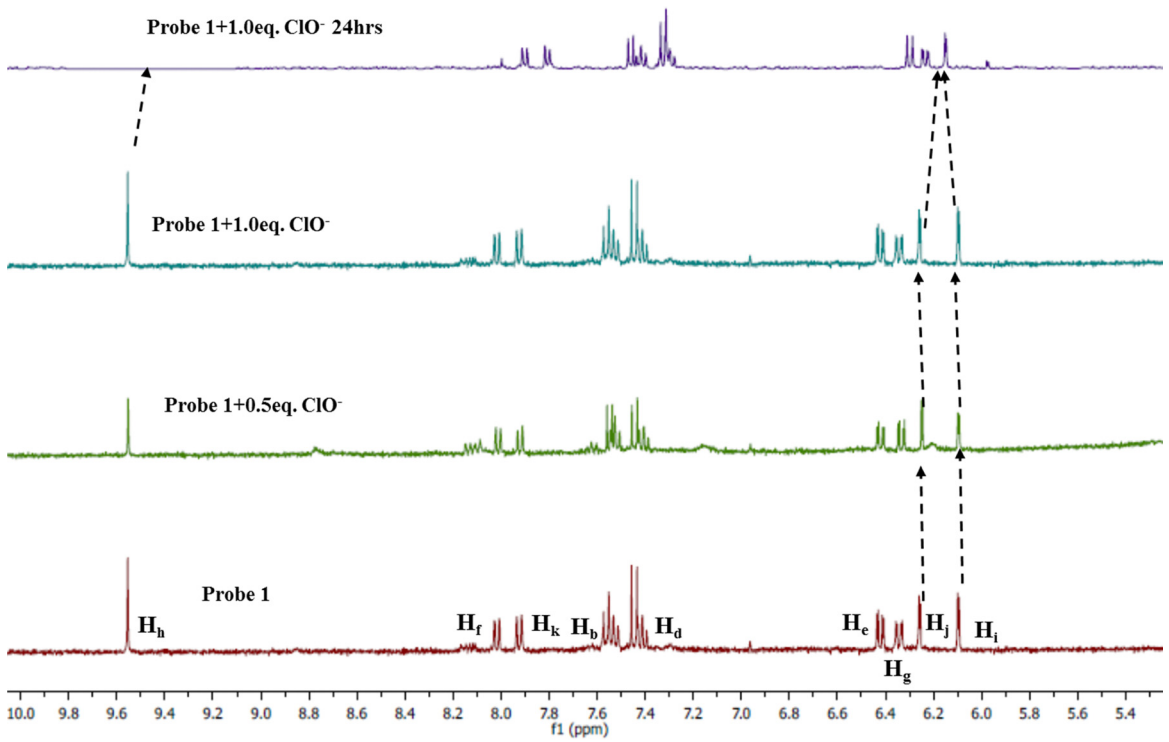

Fig. 7 Stacked ^{1}H NMR spectra of **probe 1** (5×10^{-3} M) upon addition of 1.0 eq. of ClO^- ions in CD_3OD-d_4.

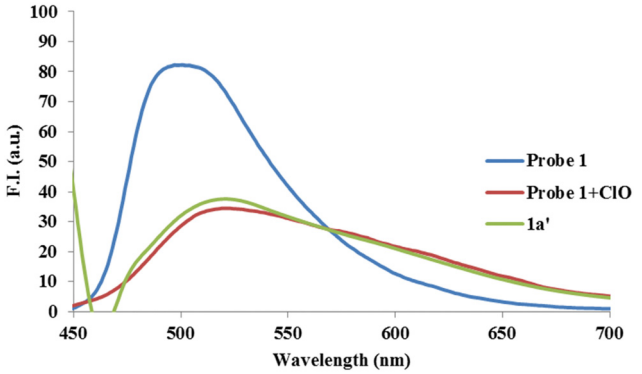

Fig. 8 Emission spectra of **probe 1**, **probe 1** + ClO^- complex and **1a**′.

addition of 1.0 eq. of ClO^- to the solution of **probe 1**, the spectrum was not affected but after 24 h the imine peak at δ 9.56 ppm disappeared, which confirmed the hydrolysis of the Schiff base (Fig. 7). The aromatic protons also showed a downfield shift upon addition of 1.0 eq. of ClO^- ions with slight splitting of the signals. The ^1H NMR titrations clearly showed that the fluorescence quenching of **probe 1** is due to the ClO^- prompted hydrolysis leading to the cleavage of the imine bond to generate an aldehyde and amine. To further confirm the hydrolysis mechanism, we took the absorption and emission spectra of the amine formed and this supported the hydrolysis mechanism (Fig. 8 and Fig. S5, ESI†). The ^1H NMR titrations clearly showed that the fluorescence quenching of **probe 1** is due to ClO^- prompted hydrolysis leading to the cleavage of the imine bond to generate aldehyde and amine (Scheme 2). The HRMS peaks at 243.0593 due to amine and 194.1180 due to aldehyde also confirmed the hydrolysis mechanism (Fig. S6, ESI†).

3.7. ClO^- detection in the solid state

Based on the above outcomes, we postulated that **probe 1** in the presence of ClO^- ions in $CH_3OH:H_2O$ (9 : 1, [v/v]) underwent a hydrolysis process. So, we predicted that on addition of ClO^- ions to **probe 1**, it should undergo some morphological changes in the solid state. The self-assemblies of **probe 1** and **probe 1** + ClO^- mixture in $CH_3OH:H_2O$ (9 : 1, [v/v]) were studied using microscopic techniques to determine any such impact on **probe 1** in the solid state owing to the addition of ClO^- ions. Field emission scanning electron microscopy (FESEM) images of a thin coating on carbon tape prepared by the drop cast method of **probe 1** in $CH_3OH:H_2O$ (9 : 1, [v/v]) revealed fibre-like aggregates all over the surface (Fig. 9a and b). These fibre-like aggregates showed an average size of 865 nm. On the other hand, the FESEM images of **probe 1** + ClO^- mixture in $CH_3OH:H_2O$ (9 : 1, [v/v]) demonstrated a flower-shaped aggregate morphology with a particle size of 955 nm (Fig. 9d and e).

The dynamic light scattering (DLS) technique further supported the increase in the particle size of **probe 1** and the probe **1** + ClO^- mixtures. The DLS of **probe 1** (20 μM) in $CH_3OH:H_2O$ (9 : 1, [v/v]) showed that the average particle size is 500–1500 nm approximately (Fig. 9c) whereas the average particle size of the **probe 1** + ClO^- mixture in $CH_3OH:H_2O$ (9 : 1, [v/v]) is 200–2000 nm approximately (Fig. 9f).

3.8. Effect of pH on probe 1

We also checked the pH stability of **probe 1** and its complex with the ClO^- ions. To check the pH stability, we performed acid–base titration. It is clear that **probe 1** was stable in the pH range from 5–10. The stability of **probe 1** in the pH range 5–10 establishes its applicability for rapid monitoring in environmental and biological backgrounds (Fig. 10). The complex of **probe 1** and ClO^- ions was also stable in the pH range from 3–11, so the detection of these ions using **probe 1** could be well performed in this pH range.

3.9. Time-correlated single photon counting (TCSPC) study

To get further insight of **probe 1** behavior towards ClO^- ions we performed time resolved fluorescence spectroscopy at 500 nm wavelength. The decay behavior of **probe 1** and its ClO^- ion complex is best fitted in the third exponential function. The average decay time for **probe 1** was found out to be 0.05 ns and it has three lifetime components of 0.77 ns (~28.75%), 2.86 ns (~18.3%) and 0.03 ns (~52.95%). After the addition of ClO^- ions, the average lifetime increased to 0.71 ns with three lifetime components of 0.93 ns (~12.45%), 1.61 ns (~83.77%) and 0.05 ns (~3.78%) (Fig. 11). The increase in the average lifetime of **probe 1** after binding with ClO^- ions suggests the dynamic quenching behavior.

3.10. Cell viability

We examined the *in vitro* detection of ClO^- ions using a cell-based system in the A549 lung cancer cell line for the possible biological applicability of **probe 1** and to determine whether the **probe 1** can specifically detect ClO^- ions under physiological conditions. We chose lung cancer cells (A549) since they are responsible for the greatest number of cancer related deaths. The cell viability experiment was performed to check the cytotoxicity of **probe 1** on the cancer cell line. The cell viability assay showed that **probe 1** is statistically non-significantly cytotoxic in nature, where 0.6%, 4.2%, 6.1%, 6.5% and 8.9%

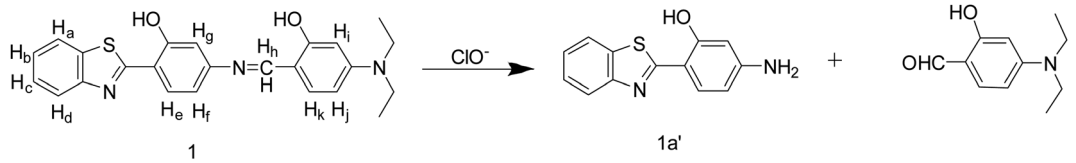

Scheme 2 Plausible sensing mechanism of ClO^- by **probe 1**.

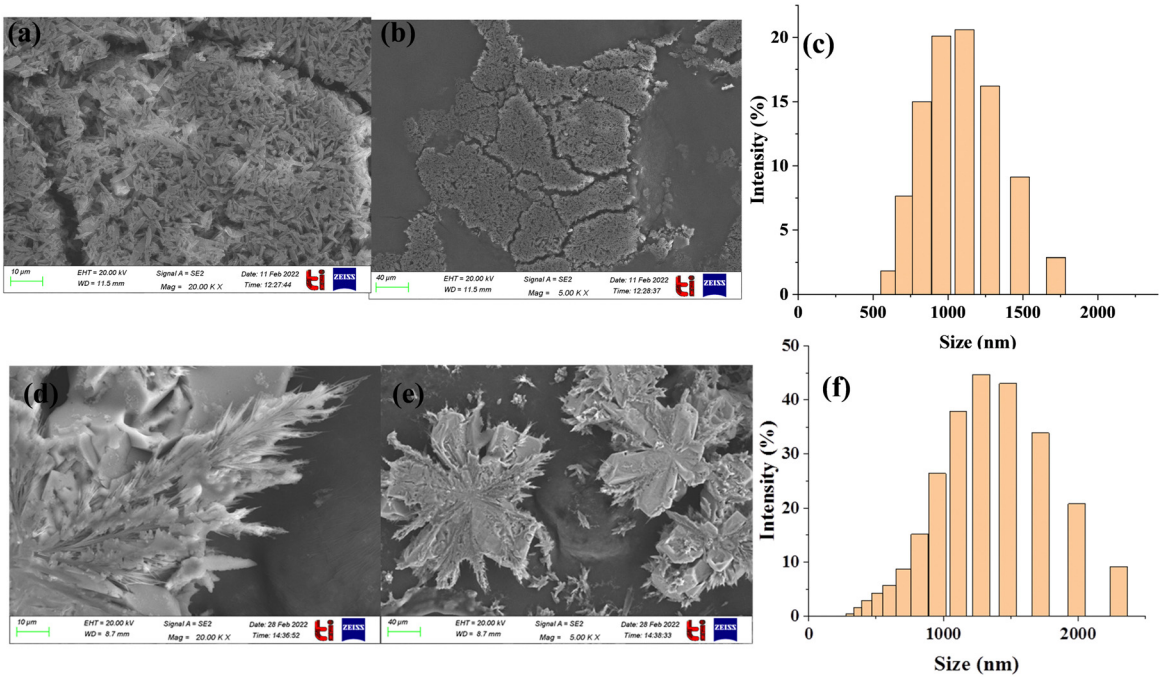

Fig. 9 (a) and (b) FE-SEM images for self-assembled fibre-like aggregates of **probe 1** (20 μM) in $CH_3OH : H_2O$ (9 : 1); (c) DLS analysis of **probe 1** (20 μM) in $CH_3OH : H_2O$ (9 : 1) solution; (d) and (e) FE-SEM images of morphological changes in **probe 1** (20 μM) after the addition of ClO^- ions in $CH_3OH : H_2O$ (9 : 1) solution; (f) DLS analysis of **probe 1** (20 μM) after the addition of ClO^- ions in $CH_3OH : H_2O$ (9 : 1) solution.

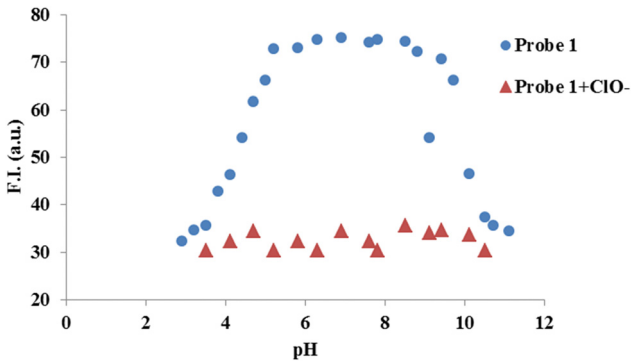

Fig. 10 Effect of pH on emission spectra of **probe 1** (20 μM) and its complex with ions in $CH_3OH : H_2O$ (9 : 1, [v/v]) at 520 nm.

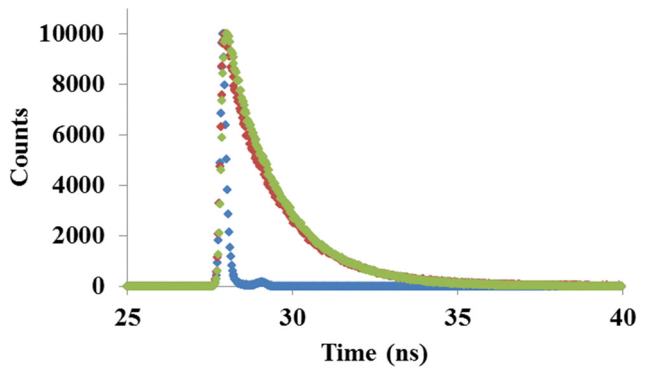

Fig. 11 Time resolved fluorescence decay of **probe 1** and **probe 1** + ClO^-.

less cell survival/growth was found due to the treatment of 1, 5, 10, 25 and 50 μM concentrations of **probe 1**, respectively. Hypochlorite is known for its cytotoxic effect and showed up to a 17.6% loss of cell viability at 100 μM hypochlorite concentration. **Probe 1** was also checked for toxicity in combination with hypochlorite where different concentrations (5, 10, 25 and 50 μM) of hypochlorite were treated with 10, 25 and 50 μM concentrations of **probe 1** (Fig. 12). A slight decrement in the cell viability was observed where the viability of cells decreased from 91.5% to 76.1% with increasing hypochlorite concentration at 25 μM **probe 1** concentration. A similar trend was observed for the **probe 1** concentration at 50 μM where the viability of the cells decreased from 98.6% to 77.5% with increasing hypochlorite (ClO^-) concentration.

3.11. *In vitro* bioimaging

It has been observed that cancer cells have elevated levels of oxidative stress and hence have more ClO^- levels when compared with normal cells. Lung carcinoma epithelial cell lines (A549) were used to study the effect of **probe 1** where the cells were cultured until they reached a confluency of 70–80% and then incubated with **probe 1** (30 μM) and ClO^- (0–100 μM) for 3 h. Cellular imaging shows the good permeability of **probe 1** with bluish-green fluorescence in the cytosol, which is localized near the nucleus, with pixel intensity of 2.47×10^5 and very little red fluorescence with pixel intensity of 0.67×10^5 which was observed due to the presence of intrinsic hypochlorite (Fig. 13A). On addition of extrinsic hypochlorite in the form of NaOCl, the red fluorescence increased with maximum pixel

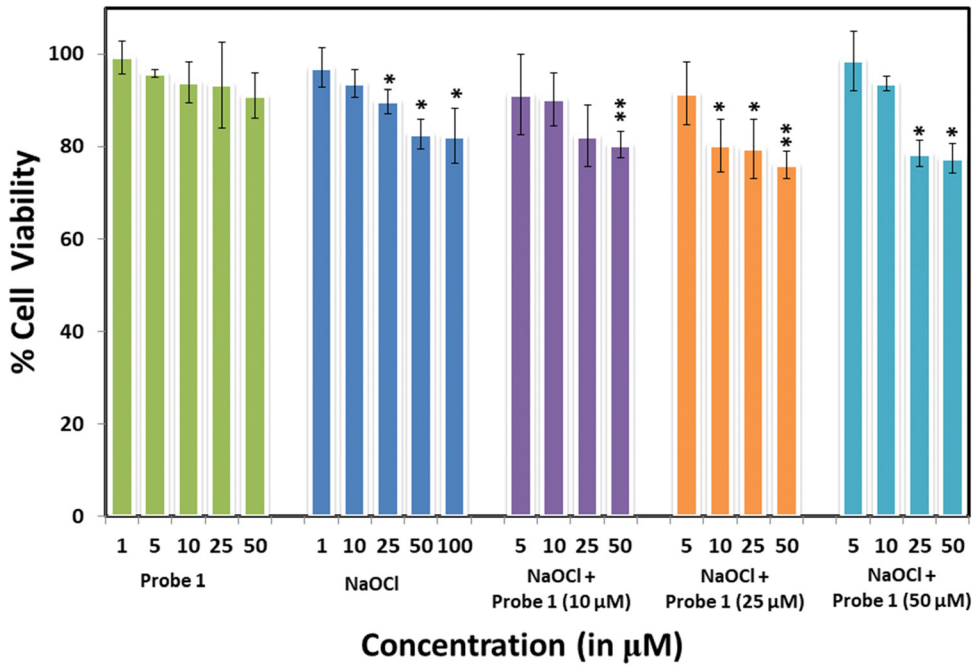

Fig. 12 Biocompatibility of **probe 1** and NaOCl.

intensity of 3.1×10^5 at ClO^- concentration of 100 μM and bluish-green fluorescence first increases with pixel intensity up to 4.0×10^5 at 5 μM ClO^- concentration and then decreases, showing pixel intensity of 1.6×10^5 at 100 μM ClO^- concentration. An exponential increase in red fluorescence was observed with pixel intensity of 3.08×10^5 up to 10 μM ClO^- concentration and thereby saturation was observed (Fig. 13B–I).

Pixel intensity was measured for the bluish-green and red fluorescence, which showed an increase in bluish-green fluorescence with increasing ClO^- concentration. After 5 μM,

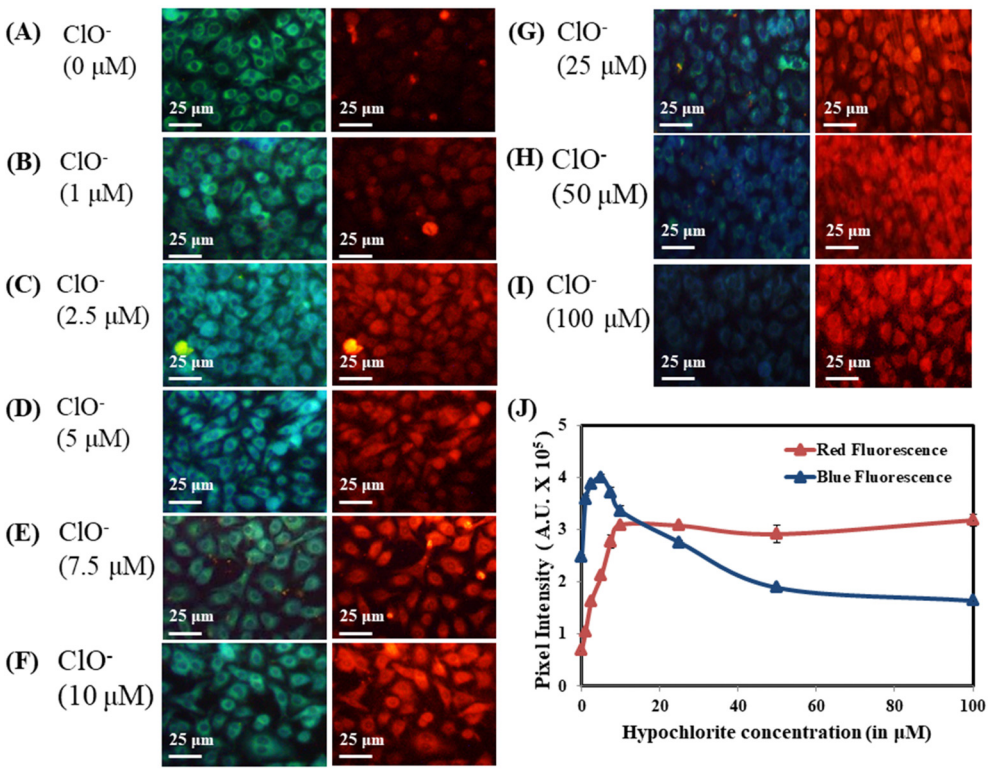

Fig. 13 *In vitro* biosensing of hypochlorite using **probe 1** (Scheme 1) (A–I) at different concentrations and (J) exponential increase in red fluorescence.

a decrease in intrinsic fluorescence was observed. On the other hand, an exponential increase in red fluorescence was observed up to 10 μM ClO^- concentration after which saturation was observed (Fig. 13J). The minimum detection limit of hypochlorite was observed at 2.5 μM for 30 μM **probe 1** concentration, where quenching in green fluorescence was observed at 25 μM. The results clearly showed that **probe 1** can detect ClO^- ions in A549 at concentrations as low as 2.5 μM.

4. Conclusion

In conclusion, we have designed and synthesized a Schiff base **probe 1** for the detection of hypochlorite (ClO^-) ions with high selectivity and sensitivity in CH_3OH–H_2O solution. **Probe 1** displayed an absorption peak at 410 nm and weak emission peak at 500 nm. The absorption and emission bands of **probe 1** showed a bathochromic shift after the addition of ClO^- ions. The lowest detection limit for ClO^- ions was calculated to be 5.5 μM. The **probe 1** has good application in biological imaging with very low cytotoxicity. The sensing mechanism was also investigated using ^1H NMR titrations.

Author contributions

Aastha Palta: data curation; formal analysis; methodology; software; roles/writing – original draft; Gulshan Kumar: theoretical studies, software, writing – original draft; Sunidhi Sharma: data curation; formal analysis; methodology; software; roles/writing – original draft; Diptiman Choudhury: conceptualization, supervision; validation; visualization; writing – review & editing. Vijay Luxami: conceptualization; funding acquisition; investigation; project administration; supervision; validation; visualization; writing – review & editing.

Ethical approval

This dataset is not applicable.

Data availability

The data supporting this article have been included as part of the ESI.†

Conflicts of interest

The authors declare no competing financial interest.

Acknowledgements

VL thanks, SERB, New Delhi (EMR/2016/002464) for financial assistance. We are thankful to SAI labs, Thapar Institute of Engineering and Technology, Patiala for NMR. Thapar Institute of Engineering and Technology, Patiala is also acknowledged for the FESEM and HRMS (DST-FIST(SR/FST/CS-II/2018/69) facilities.

References

1 T. Aoki and M. Munemori, *Anal. Chem.*, 1983, **55**, 209–212.
2 E. T. Chouchani, L. Kazak, M. P. Jedrychowski, G. Z. Lu, B. K. Erickson, J. Szpyt, K. A. Pierce, D. Laznik-Bogoslavski, R. Vetrivelan and C. B. Clish, *Nature*, 2016, **532**, 112–116.
3 X. He, H. Chen, C. Xu, J. Fan, W. Xu, Y. Li, H. Deng and J. Shen, *J. Hazard. Mater.*, 2020, **388**, 122029.
4 Y. Zhu, Y. Ma, Y. Liu, Z. Liu, S. Ma, M. Xing, D. Cao and W. Lin, *Sens. Actuators, B*, 2021, **327**, 128848.
5 S. Di Meo, S. Iossa and P. Venditti, *J. Endocrinol.*, 2017, **233**, R15–R42.
6 Z. Liang, T.-H. Tsoi, C.-F. Chan, L. Dai, Y. Wu, G. Du, L. Zhu, C.-S. Lee, W.-T. Wong and G.-L. Law, *Chem. Sci.*, 2016, **7**, 2151–2156.
7 F. C. Fang, *Nat. Rev. Microbiol.*, 2004, **2**, 820–832.
8 D. Vara and G. Pula, *Curr. Mol. Med.*, 2014, **14**, 1103–1125.
9 A. Strzepa, K. A. Pritchard and B. N. Dittel, *Cell. Immunol.*, 2017, **317**, 1–8.
10 C. L.-L. Chiang, L. E. Kandalaft, J. Tanyi, A. R. Hagemann, G. T. Motz, N. Svoronos, K. Montone, G. M. Mantia-Smaldone, L. Smith and H. L. Nisenbaum, *Clin. Cancer Res.*, 2013, **19**, 4801–4815.
11 M. Ren, K. Zhou, L. He and W. Lin, *J. Mater. Chem. B*, 2018, **6**, 1716–1733.
12 D. Cao, Z. Liu, P. Verwilst, S. Koo, P. Jangjili, J. S. Kim and W. Lin, *Chem. Rev.*, 2019, **119**, 10403–10519.
13 Y. L. Pak, S. J. Park, Q. Xu, H. M. Kim and J. Yoon, *Anal. Chem.*, 2018, **90**, 9510–9514.
14 X.-L. Hao, L. Zhang, D. Wang, C. Zhang, J.-F. Guo and A.-M. Ren, *J. Phys. Chem. C*, 2018, **122**, 6273–6287.
15 T. Fukuyama, B. Martel, K. Linder, S. Ehling, J. Ganchingco and W. Bäumer, *Clin. Exp. Allergy*, 2018, **48**, 78–88.
16 M. Boncler, B. Kehrel, R. Szewczyk, E. Stec-Martyna, R. Bednarek, M. Brodde and C. Watala, *Int. J. Biol. Macromol.*, 2018, **107**, 2701–2714.
17 R. Jeelani, D. Maitra, C. Chatzicharalampous, S. Najeemuddin, R. T. Morris and H. M. Abu-Soud, *J. Pineal Res.*, 2018, **64**, e12463.
18 I. Q. Tantry, S. Waris, S. Habib, R. H. Khan, R. Mahmood and A. Ali, *Int. J. Biol. Macromol.*, 2018, **106**, 551–558.
19 H. Feng, Z. Zhang, Q. Meng, H. Jia, Y. Wang and R. Zhang, *Adv. Sci.*, 2018, **5**, 1800397.
20 X. He, C. Wu, Y. Qian, Y. Li, F. Ding, Z. Zhou and J. Shen, *Talanta*, 2019, **205**, 120118.
21 S. Feng, D. Liu, W. Feng and G. Feng, *Anal. Chem.*, 2017, **89**, 3754–3760.
22 S. Xu, H.-W. Liu, X. Yin, L. Yuan, S.-Y. Huan and X.-B. Zhang, *Chem. Sci.*, 2019, **10**, 320–325.
23 B. Yun, K. D. Roberts, P. E. Thompson, R. L. Nation, T. Velkov and J. Li, *Sensors*, 2017, **17**, 2598.
24 K. Kumar, S. Kaur, S. Kaur, G. Bhargava, S. Kumar and P. Singh, *J. Mater. Chem. B*, 2020, **8**, 125–135.
25 L. Chen, S. J. Park, D. Wu, H. M. Kim and J. Yoon, *Dyes Pigm.*, 2018, **158**, 526–532.
26 S. Sun, K. M. Błażewska, A. P. Kadina, B. A. Kashemirov, X. Duan, J. T. Triffitt, J. E. Dunford, R. G. G. Russell,

F. H. Ebetino and A. J. Roelofs, *Bioconjugate Chem.*, 2016, **27**, 329–340.
27 J. Zhang, K.-L. Wong, W.-K. Wong, N.-K. Mak, D. W. Kwong and H.-L. Tam, *Org. Biomol. Chem.*, 2011, **9**, 6004–6010.
28 Q. Zhang, P. Zhang, Y. Gong and C. Ding, *Sens. Actuators, B*, 2019, **278**, 73–81.
29 J. Zha, B. Fu, C. Qin, L. Zeng and X. Hu, *RSC Adv.*, 2014, **4**, 43110–43113.
30 Y. Wu, J. Wang, F. Zeng, S. Huang, J. Huang, H. Xie, C. Yu and S. Wu, *ACS Appl. Mater. Interfaces*, 2016, **8**, 1511–1519.
31 B. Wang, F. Zhang, S. Wang, R. Yang, C. Chen and W. Zhao, *Chem. Commun.*, 2020, **56**, 2598–2601.
32 J. Gong, M. Yu, C. Wang, J. Tan, S. Wang, S. Zhao, Z. Zhao, A. Qin, B. Tang and X. Zhang, *Chem. Commun.*, 2019, **55**, 10768–10771.
33 C. Duan, M. Won, P. Verwilst, J. Xu, H. S. Kim, L. Zeng and J. S. Kim, *Anal. Chem.*, 2019, **91**, 4172–4178.
34 Y. Koide, Y. Urano, K. Hanaoka, T. Terai and T. Nagano, *J. Am. Chem. Soc.*, 2011, **133**, 5680–5682.
35 S. Enbanathan, S. Manickam, S. Munusamy, D. Jothi, S. M. Kumar and S. K. Iyer, *New J. Chem.*, 2022, **46**, 6570–6576.
36 E. Barni, P. Savarino, M. Marzona and M. Piva, *J. Heterocycl. Chem.*, 1983, **20**, 1517–1521.
37 R. Mehta, P. Kaur, D. Choudhury, K. Paul and V. Luxami, *J. Photochem. Photobiol., A*, 2019, **380**, 111851.
38 S. Sharma, V. Goel, P. Kaur, K. Gadhave, N. Garg, L. D. Singla and D. Choudhury, *Exp. Parasitol.*, 2023, **253**, 10859.
39 P. Kaur and D. Choudhury, *J. Drug Targeting*, 2021, **29**, 541–550.
40 P. Kaur, S. Sharma, S. D. Choudhury, D. Singh, S. Sharma, K. Gadhave, N. Garg and D. Choudhury, *Colloids Surf., B*, 2020, **188**, 110785.
41 V. Goel, S. Sharma, N. K. Chakroborty, L. D. Singla and D. Choudhury, *Heliyon*, 2023, **9**, e13699.